MTLA 50 (2026) 102940

Contents lists available at ScienceDirect

Materialia

journal homepage: www.elsevier.com/locate/mtla

Full Length Article

Hierarchical phase formation in tungsten heavy alloys fabricated via laser powder bed fusion

Anugrahaprada Mukundan [a,*], Ryosuke Ozasa [b], Takayoshi Nakano [b], Mitsuhiro Murayama [a,c,*]

[a] Materials Science and Engineering Department, Virginia Polytechnic Institute and State University, Blacksburg, VA, 24061, USA
[b] Division of Materials and Manufacturing Science, Graduate School of Engineering, The University of Osaka, Suita, Osaka, 565-0871, Japan
[c] Institute for Materials Chemistry and Engineering, Kyushu University, Kasuga, Fukuoka, 816-8580, Japan

ARTICLE INFO

Keywords:
Tungsten heavy alloys
Laser powder bed fusion
Nanoscale microstructure characterization
Microstructure inhomogeneity
Solute enriched regions
Laves phase

ABSTRACT

Additive manufacturing (AM) of tungsten heavy alloys (WHAs) is of interest, given its ability to fabricate components with complex geometries compared to conventional powder metallurgy (PM) for various high-temperature, structural applications. Previous research on AM WHAs primarily focused on optimizing processing conditions to produce high density parts with minimal defects. However, an in-depth understanding of the nanoscale microstructure in these alloys under non-equilibrium rapid solidification AM conditions remains insufficiently explored.

This study investigates the influence of processing on the microstructure of AM WHAs using a laser powder bed fusion (LPBF) fabricated 90W-7Ni-3Fe alloy through multiscale characterization. Scanning electron microscopy (SEM) imaging revealed microscale inhomogeneity, suggesting location dependent variations in thermal gradients during LPBF. Further, a randomly oriented equiaxed grain structure was observed, implying that alloying W with Ni and Fe promotes textured columnar to random equiaxed transition, under these solidification conditions. Transmission electron microscopy (TEM) provided further insight into crystallographic defects in the form of high dislocation density, and phase transformations in the form of solute-enriched regions and nano-sized Fe_2W precipitates in some matrix regions. The Fe_2W Laves phase was previously unobserved in PM WHAs and could indicate local variations in the composition and equilibrium conditions of the matrix. Though known to be a brittle phase, Fe_2W is expected to strengthen the WHA through Orowan mechanisms when present as nano-sized precipitates and could indicate advantages of AM processing. These nanoscale findings, not previously observed by SEM, provide a foundation to link the processing, microstructure, and ultimately performance of AM WHAs.

1. Introduction

WHAs are two-phase metal-metal composites (MMCs) fabricated by adding small amounts of alloying elements such as Ni, Fe or Cu (typically a few weight percent) into W. These alloys have high density, good mechanical strength, good corrosion resistance, and improved machinability and room temperature ductility compared to pure W. These properties make WHAs candidates for various structural applications such as in aircraft engine parts like flywheels, rotors and counterweights, as radiation shields in medical equipment, and as plasma facing material components in nuclear fusion reactors [1].

Powder Metallurgy (PM) techniques such as Liquid Phase Sintering (LPS) have successfully been used to fabricate high density WHAs in the past. However, additive manufacturing (AM) is an emerging alternative to fabricate WHAs because of its ability to print parts with complex geometries in a layer-by-layer fashion. AM parts are known to have defects such as lack of fusion and porosity, which result in them not being fully dense; however, these defects can be mitigated through processing parameter optimization [2]. In addition, the ability to tune these processing parameters can be used to design the local and/or bulk material microstructure, and consequently, its mechanical behavior. This capability makes AM a viable alternative to fabricate WHAs that are

* Corresponding authors at: Materials Science and Engineering Department, Virginia Polytechnic Institute and State University, Blacksburg, VA, 24061, USA.
E-mail addresses: anugrahaprada@vt.edu (A. Mukundan), ozasa@mat.eng.osaka-u.ac.jp (R. Ozasa), nakano@mat.eng.osaka-u.ac.jp (T. Nakano), murayama@vt.edu (M. Murayama).

https://doi.org/10.1016/j.mtla.2026.102940
Received 24 June 2026; Accepted 27 October 2026
Available online 27 October 2026
2589-1529/© 2026 The Authors. Published by Elsevier Inc. on behalf of Acta Materialia Inc. This is an open access article under the CC BY license (http://creativecommons.org/licenses/by/4.0/).

suitable for various structural applications.

There is substantial research demonstrating the successful fabrication of W and WHA components using AM, particularly laser-based AM techniques. Among these studies, Ivekovic et al. used different LPBF parameters to print 90W-7Ni-3Fe and investigated the effect of processing parameters. They identified three bonding mechanisms depending on input laser energy density [3]. Wang et al. studied microstructure evolution and strengthening mechanisms in WHAs fabricated using laser melting deposition (LMD). They reported an improvement in tensile strength and hardness of the WHA specimens due to grain refinement during LMD [4]. Schwanekamp et al. evaluated the influence of LPBF parameters and heat treatment on W-Ni-Fe alloys with 90% and 95% W. They obtained microstructures similar to LPS WHAs with their heat treatment strategy [5]. Verdonik et al. observed differences in 93W-5.6Ni-1.4Fe WHA microstructure by changing powder morphology and LPBF parameters and suggested optimum parameters to minimize the problem of poor wettability of W [6]. Dai et al. implemented dual-laser LPBF to print high-density, nearly microcrack free 98W-Ni-Fe alloy and observed finer, equiaxed grains which controlled microcrack propagation at grain boundaries [7].

Much of the existing research on AM of WHAs has focused on understanding how AM processing parameters and thermal post treatments influence the microstructure and mechanical properties of these alloys. Researchers also emphasized optimizing processing conditions to achieve high-density parts with reduced defects. However, opportunities remain to further understand the non-equilibrium rapid solidification kinetics and phase transformation in these alloys at the nanoscale. Therefore, this work aims to explore microstructure evolution through multiscale characterization by examining the rapid solidification characteristics of AM fabricated WHAs at the nanoscale. A combination of SEM and TEM techniques were utilized to gain nanoscale insight into phase distribution, dislocation structures, and precipitate morphology. These nanoscale findings will be helpful to understand processing-structure- performance relationships in AM fabricated WHAs, which will subsequently aid in microstructure driven design of these alloys.

2. Experimental procedure

Spherical tungsten (Tekna, Norway), nickel (Sanyo Special Steel, Japan) and iron (Sanyo Special Steel, Japan) powders with >99.5% purity were used in a 90:7:3 ratio by weight respectively. These powders were mixed in the Aichi RM-10 rocking mixer for 12 h to achieve homogeneity. The final powder composition was evaluated using Energy dispersive x-ray spectroscopy (EDS) as shown in Fig. 1. The particle size distribution of the final powders was measured using a Malvern Panalytical Mastersizer 3000E and a D_{50} of 33.3 μm was reported.

These powders were used to print 5 × 5 × 10 mm blocks using the EOS M290 LPBF machine. The specimens were fabricated in an Ar atmosphere using a Yb-fiber laser. Laser power of 360 W and scanning speed of 800 mm/s was used to fabricate WHA blocks layer-by-layer with a hatch spacing of 40 μm, and layer of thickness of 20 μm, using a bidirectional scanning strategy with a misorientation of 67° between consecutive layers. Fig. 2(a) represents the laser scanning path and build direction. A carbon steel baseplate maintained at 200 °C was used to suppress the generation of residual stress in the printed specimens. The measured relative density of the specimen was 99.07%.

Specimens for X-ray diffraction (XRD), SEM, electron backscatter diffraction (EBSD) and TEM characterization were cut from the LPBF blocks to observe the YZ and XY planes, as shown in Fig. 2(b). XRD, SEM and EBSD specimens were prepared through grinding and polishing using lapping films and colloidal silica suspension, respectively until a mirror polished surface was obtained. XRD was performed using the Malvern Panalytical Aeris benchtop diffractometer operated at 40 kV, 7.5 mA and a Cu anode ($\lambda_{K\alpha} = 0.1541$ nm). The scan range was 5–90° with a step of 0.01°. The specimen surfaces were examined by SEM and EBSD using the ThermoFisher Scientific Helios 5 UC Dual Beam.

Specimens for TEM were prepared by thinning to a thickness of roughly 65 μm, followed by double-sided dimple grinding with colloidal diamond suspension on a Gatan model 656 dimple grinder. The specimens were finished by ion milling using the Gatan PIPS II Precision Ion Polishing using a liquid nitrogen cooling stage and were examined using the JEOL JEM 2100 TEM. EDS was also performed on the TEM specimens for composition analysis.

Room temperature Vickers hardness tests were carried out on the YZ and XY planes using a LECO LV700 AT hardness tester. A 1 kgf load with a dwell time of 10 s was used for the tests, and 10 indents were made on each specimen.

3. Results

3.1. XRD characterization

The XRD results shown in Fig. 3. shows peaks corresponding primarily to the BCC W and FCC γ phases. The spectrum suggests that no intermetallic phases were detected within the detection limits of the XRD.

3.2. SEM characterization

Fig. 4. shows secondary electron (SE) SEM images giving an overview of the WHA microstructure, looking at the XY and YZ planes. Two distinct microstructures can be observed: one region with nearly spherical, un-melted W particles in a γ matrix (dark contrast surrounding W regions in Fig. 4), similar to the composite structure in conventional LPS WHAs [8] and the other region with a uniform structure, suggesting complete melting of powders. The un-melted W particle region spans about 100 μm from start/end of track regions in the bidirectional scanning pattern.

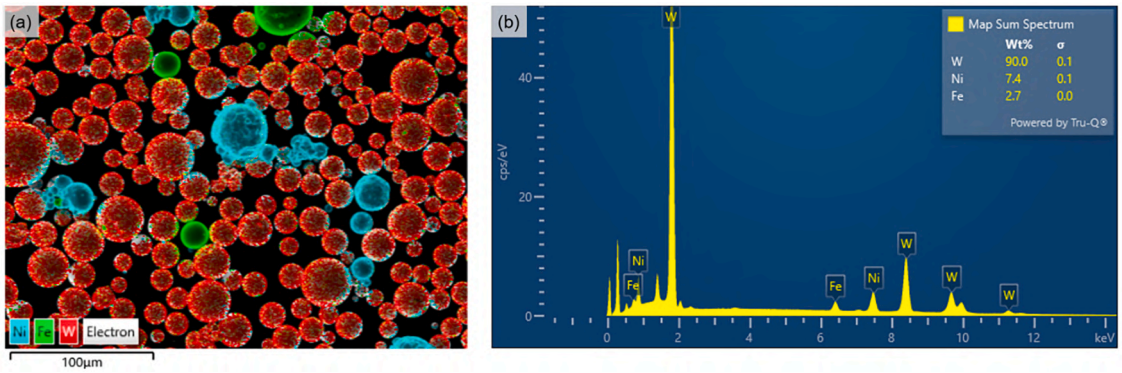


Fig. 1. Composition analysis of powders showing distribution of W, Ni, and Fe (a) EDS map (b) Corresponding EDS spectrum.

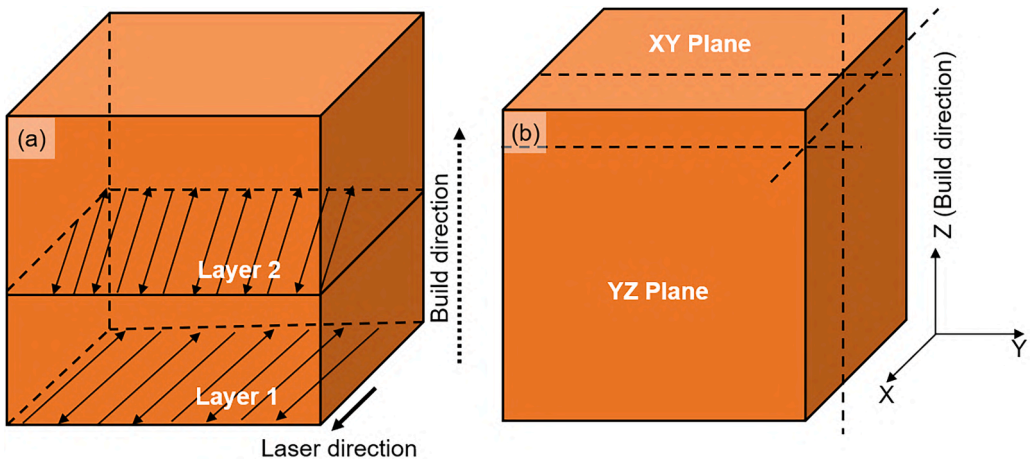


Fig. 2. Schematic diagram showing (a) laser path and build direction, layers 1 and 2 have an interlayer rotation of 67° (b) specimen observation directions.

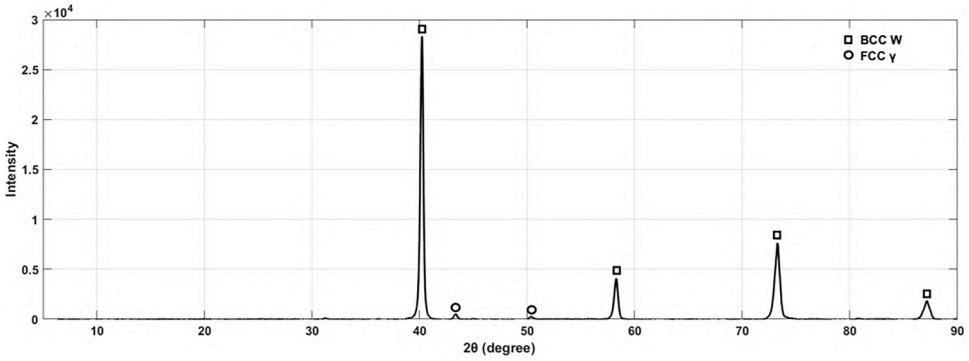


Fig. 3. XRD spectrum showing phases present in the LPBF WHA.

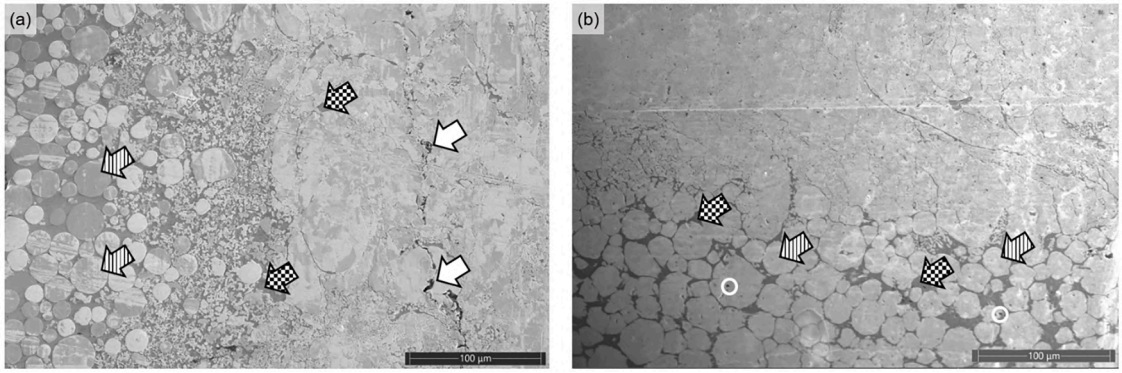


Fig. 4. SE images of the WHA (a) XY plane (b) YZ plane. Striped arrows show un-melted W particles; checkered arrows show the matrix. Solid arrows and circles show cracks and pores, respectively.

Fig. 5 presents backscatter electron (BSE) SEM images, further highlighting microstructural features such as W dendrites in the γ matrix and submicron scale γ precipitates, which appear as dark, dot-like features present in W grains. It is observed from Figs. 4 and 5 that W dendrites are primarily located in regions with un-melted W particles. This observation implies that un-melted W particles act as favorable sites for the heterogenous nucleation and growth of W dendrites. Previous studies on AM WHAs refer to this process as reprecipitation, during which dissolved W reprecipitates on un-melted W particles [4,9]. The formation of γ precipitates indicates that the processing conditions used allowed complete melting of the powders and aided in the evaporation of the matrix, forming these precipitates in W grains [3].

Additionally, Figs. 4 and 5 highlight processing defects such as cracks and pores present in the specimen. Based on SEM image processing, these defects collectively occupied an area fraction of about 1%. WHAs fabricated using AM are highly sensitive to microcracks due to the high cooling rate [5,7]. In addition, W exhibits room temperature brittleness, which further makes it prone to chipping, edge cracking, and surface cracks during sectioning and grinding [10,11]. Thus, it is likely that specimen preparation accentuated these pre-existing microcracks, resulting in visible cracks along the specimen edges. Porosity is a widely known defect in metal AM. Their spherical shape suggests that Ar gas entrapment during solidification resulted in the formation of pores [2]. Further, it is noted from these figures that melt pools were not observed

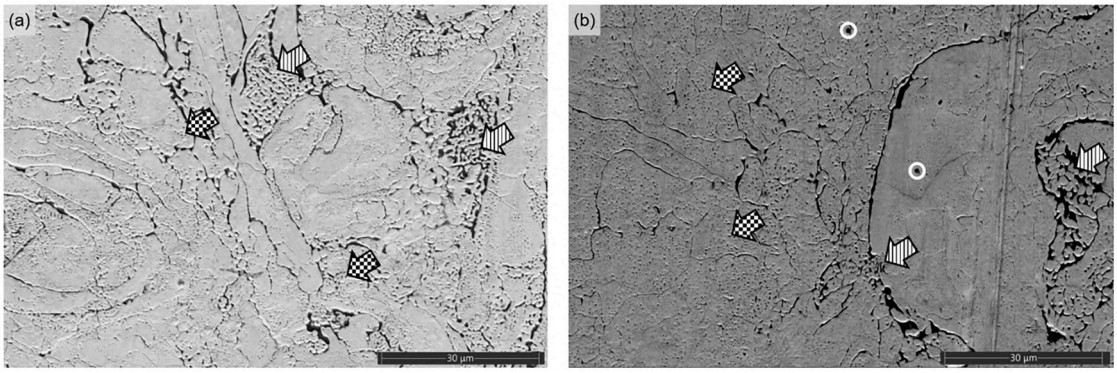


Fig. 5. BSE images of the WHA (a) XY plane (b) YZ plane. Striped arrows show W dendrites, checkered arrows show γ precipitates. Circles show pores.

during standard SEM analysis. Etching might be necessary to reveal melt pools, if present.

The grain texture, misorientation and size distribution in the as-built WHA is shown in Fig. 6. The un-indexed regions in the EBSD map (black regions in Fig. 6a) are associated with LPBF processing defects. It can be seen from the EBSD maps and the corresponding pole figures (Figs. 6a, d, S.1.) that the specimen does not show preferential texture along all directions. Previous research on laser-based AM of WHAs has also reported no preferential texture in as-built WHAs [4,12]. The presence of misorientation (with an average of 0.566°), as observed in Fig. 6b and c,

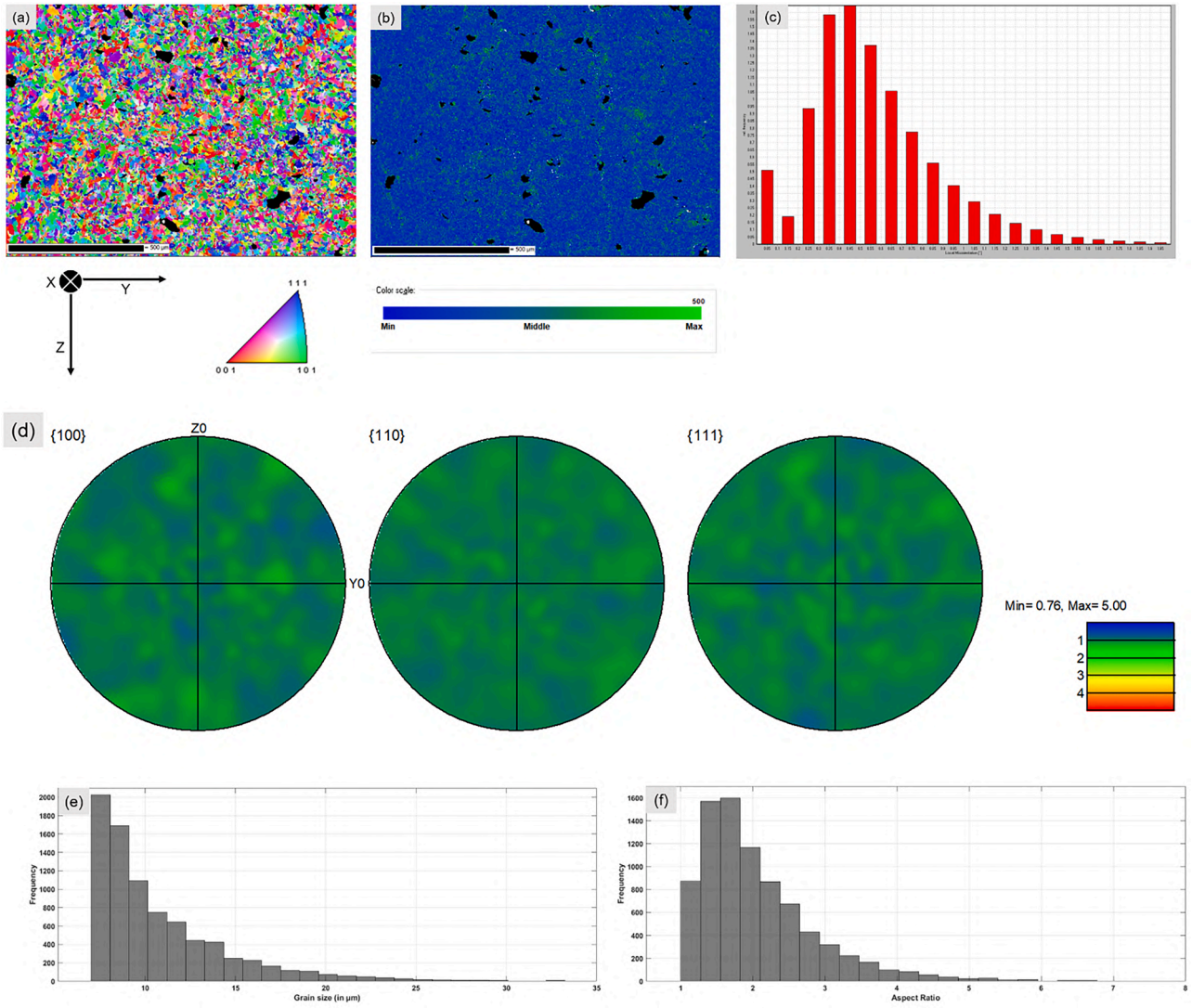


Fig. 6. (a) EBSD IPF map along build direction, Z (IPF Z) collected from the YZ plane of the as-built WHA specimen, with a 500 µm scale bar. IPF X and IPF Y can be found in Supplementary Fig. S.1. (b) Kernel Average Misorientation (KAM) map, with a 500 µm scale bar (c) Local misorientation distribution (d) Corresponding pole figures (e) Grain size distribution (f) Aspect ratio distribution.

implies that the grains experience strain which could arise either due to confinement during coarsening / growth or thermal stresses during rapid solidification. It was observed in previous research on LMD WHAs that the misorientation gradient was larger than their as-fabricated LPS counterparts [4]. The misorientation data was used to approximate the geometrically necessary dislocations (GND) density and the average GND density was calculated to be $3.062 \times 10^{13}\ m^{-2}$. Details of GND density estimation and distribution can be found in the Supplementary Section S.2. The grain size and aspect ratio distributions in Fig. 6e, f, report an average grain size and aspect ratio of 10.753 μm and 2.066, respectively, suggesting that the specimen exhibits a fine, equiaxed grain structure.

3.3. TEM characterization

SEM analysis provides insight into the overall morphology, phase distribution, and crystallographic texture of the as-printed LPBF WHA. However, this cannot resolve nanoscale features such as γ precipitates, local strain and dislocation networks, which could significantly influence mechanical behavior of WHAs. Thus, TEM characterization was performed to obtain deeper insight into the effects of rapid solidification microstructure.

Fig. 7 presents a bright field (BF) TEM micrograph, with the corresponding selected area diffraction pattern (SAED) collected from a W region, providing a closer insight into the WHA microstructure. The BF image shows that the γ precipitates are embedded in W grains and highlights the orientation of γ precipitates with respect to W. The SAED in Fig. 7(b) suggests that the BCC W and FCC γ phases are oriented such that $[011]_W \| [001]_\gamma$, however, this orientation relationship was not observed consistently across the specimen. Fig. 7(a) also shows the presence of nano-sized pores (about 100 nm), preferentially located in the γ precipitates. It is plausible that the lower melting point of the γ phase compared to W allowed gas bubbles to settle in the molten γ regions and these bubbles were entrapped during the formation of γ precipitates. These pores could act as sites of failure.

The TEM BF micrographs in Fig. 8. show high dislocation density in the specimen, where dislocations are observed to be piling up in Fig. 8 (a). The presence of dislocations in the as-built microstructure aligns with the observation of misorientation in the KAM map (Fig. 6b), confirming that laser heating and rapid solidification resulted in thermal stresses and strains in the material. High dislocation density has been previously reported in as-sintered WHAs [13] and dislocation behavior has been estimated based on EBSD misorientation and grain boundary analysis in some AM WHAs [4,7]. However, the direct observation of dislocations in LPBF WHAs at the TEM scale is novel. High dislocation density could influence mechanical behavior under external stresses.

Fig. 8(b) further shows the presence of spherical nanoscale features in the W grain, which are about 50–150 nm in size. These nano-sized features were not detected by SEM characterization and do not show a distinct SAED pattern of their own, but a BCC W diffraction pattern. However, the TEM EDS spectrum in Fig. 8(c) indicates the presence of Ni and Fe, along with W. While the strong W peak is likely from the W grain underneath, the spherical features are Ni-Fe rich regions and could be Ni-Fe enriched regions. The exact nature and structure of these features are currently under investigation.

Fig. 9 represents SAED obtained from the γ matrix region, along with TEM EDS spectra. It can be noted from the EDS spectra (Fig. 9(c, d)) that the γ matrix is primarily composed of Ni and Fe but also suggest that W dissolved into the matrix. However, W regions do not indicate as much of Ni or Fe in them (Fig. 9(e)). W-Ni and W-Fe equilibrium phase diagrams indicate that W has higher solubility in Ni and Fe compared to the negligible solubility of Ni and Fe in W, thus corroborating this observation [14,15]. Li et al. previously observed W dissolution into the matrix in WHAs fabricated using LPBF and attributed the observation to the difference in solubilities of the constituent elements [16].

Vegard's law describes a linear relationship between the lattice parameter and composition of an alloy, as follows [17]:

$$a_{AB} = x a_A + (1 - x) a_B \tag{1}$$

where x is the composition of constituent A, a_A, a_B, and a_{AB} are the lattice parameters of constituent A, B and alloy AB respectively. Approximating the γ matrix lattice parameter using Eq. (1), considering a Ni-Fe binary, a_γ should range between $a_{Ni} = 0.352\ nm$ and $a_{Fe(FCC)} = 0.365\ nm$ [18]. The calculated lattice parameter from the measured interplanar spacing from the FCC SAED (Fig. 9(b)) is approximately 0.370 nm, which is greater than this range, further confirming that the γ matrix contains small amounts of W, in addition to Ni and Fe.

Additionally, precipitates, around 100- 200 nm in size, were observed in some γ matrix regions, as seen in Fig. 10(a). Based on the EDS spectra in Fig. 10(b, c), the precipitates are W-rich, likely a W-Fe phase.

While these precipitates are too thin to obtain a distinct SAED pattern, looking closely at the precipitates (HRTEM image and its cor-

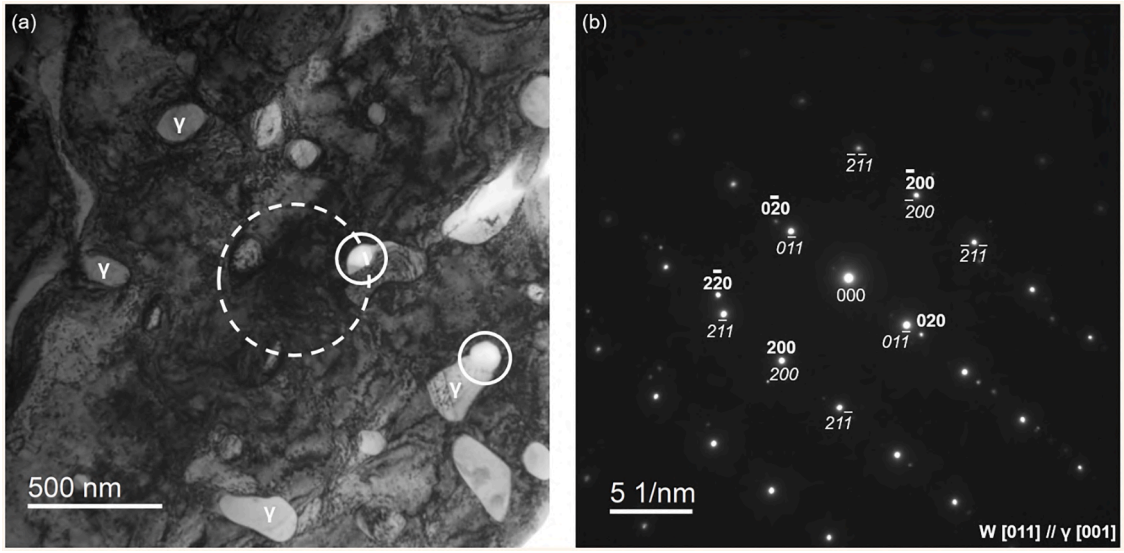


Fig. 7. (a) TEM BF image showing γ precipitates in W. The dotted circle represents the size of the aperture used to collect SAED pattern. Solid circles represent pores. (b) SAED pattern. Bold fonts represent γ spots and italicized fonts represent W spots.

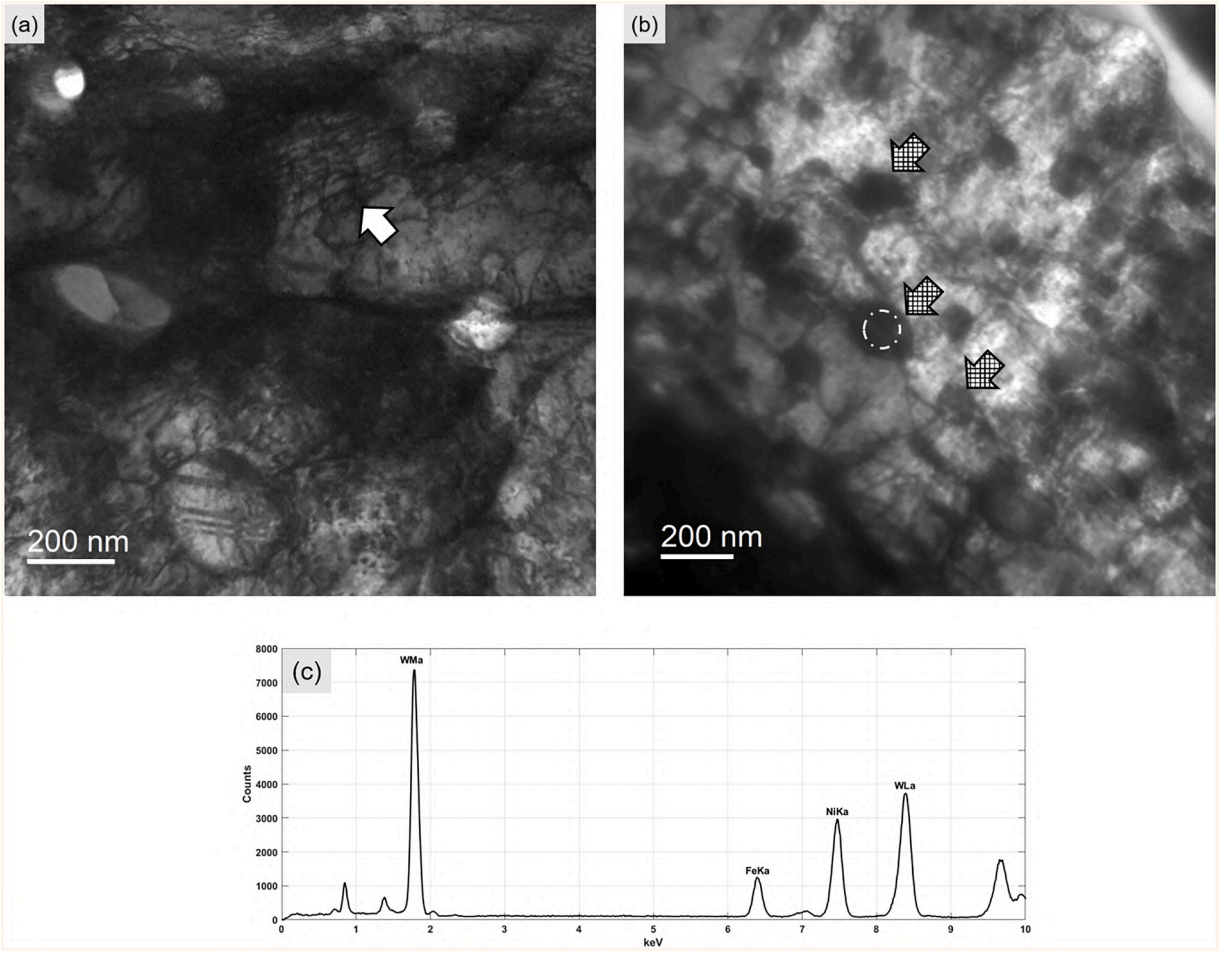


Fig. 8. TEM BF images showing (a) high density dislocations in the WHA specimen. Image taken at 60kX. Solid arrows indicate dislocations piling up. (b) Spherical nanoscale features highlighted by hatched arrows. Image taken at 50kX. (c) EDS spectrum collected from the region represented by the dash-dot circle in (b).

responding FFT in Fig. 11b, c), and comparing the observed structure to the potential W-Fe phases, it is deduced that the precipitates are the Fe_2W phase (space group $P6_3/mmc$ (194), a = 0.4743 nm, c = 0.7688 nm [19]). These precipitates were not observed in both the XRD and SEM characterization as they are below the resolution limits of these techniques.

3.4. Vickers hardness measurement

Room temperature Vickers hardness measurements were carried out on both the XY and YZ planes, with 10 indents per specimen. The measured mean hardness values with their standard deviations for the specimen are 373.92 ± 45.08 HV and 341.85 ± 38.54 HV for the XY and YZ planes, respectively. Details of hardness measurements can be found in Supplementary Material Section S.3. A comparison between Vickers hardness values previously reported for conventionally fabricated 90W-7Ni-3Fe WHAs and the present work are presented in Table 1. The present work reports an overall improvement in hardness over their conventionally fabricated counterparts, as seen in Table 1.

4. Discussion

4.1. Effect of laser scanning on the microstructure

The microstructural inhomogeneity observed in the SEM characterization (Section 3.2) suggests a dependence on the localized thermal conditions generated as a result of laser scanning during LPBF processing. The influence of laser scanning conditions on the microstructure is discussed below.

The presence of the un-melted W region, as observed in Fig. 4. is likely associated with local variations in temperature attributed to the Gaussian distribution of laser energy. Powders located near the start / end of track regions are exposed to the surrounding inert gas atmosphere compared to powders within the laser track. Further, these regions are maintained at high temperature for a shorter time than the regions within the laser track, owing to the Gaussian energy distribution. These conditions result in a steeper temperature gradient in the start / end regions of the of track, which can reduce the time available for complete melting and solidification, or for maintaining sufficiently high temperatures to promote solid state sintering among W particles, resulting in un-melted W particles in this region.

In metal AM, unstable melt pools or their absence is primarily attributed to incomplete melting of the powder bed and lack of fusion due to insufficient laser energy. Lack of fusion defects typically appear as elongated, irregular shapes in the order of 50 μm to a few mm in size [2]. However, such defects were not observed in the present work, suggesting that the absence of clear melt pool boundaries, as seen in Figs. 4 and 5, is not due to insufficient melting. Conventionally, melt pool boundaries are observed in AM alloys due to elemental segregation during solidification. However, the WHA used in this study majorly consists of W (90% by weight or 80% by volume). Further, W is expected to solidify earlier than the lower melting temperature elements, Ni and Fe, near the melt pool boundary where solidification begins. Consequently, the melt pool boundary regions primarily contain W, and the alloy does not exhibit elemental segregation, resulting in the absence of discernible melt pools. The EDS line scan in Fig. 12 confirms the absence

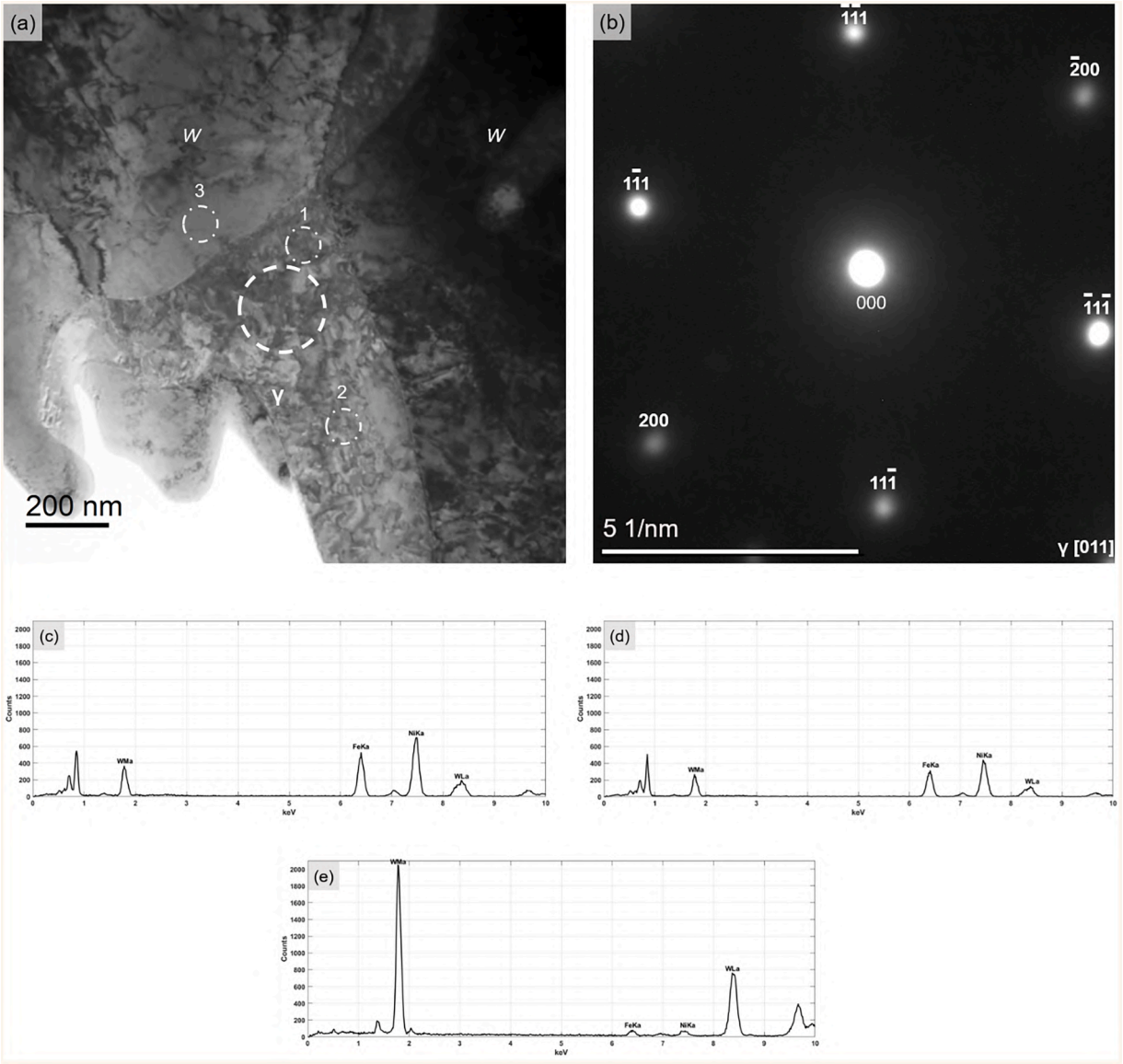


Fig. 9. (a) TEM BF image of the γ matrix. The dotted circle represents the size of the aperture used to collect the SAED pattern. Dash-dot circles represent TEM EDS spots (b) SAED pattern from the γ matrix (c) EDS spectrum from spot 1 (d) EDS spectrum from spot 2 (e) EDS spectrum from spot 3.

of elemental segregation.

4.2. Solidification considerations in LPBF WHAs

The microstructural features observed in the multiscale characterization indicates that the non-equilibrium thermal conditions during rapid solidification in LPBF play a significant role in dictating the grain structure and phase distribution in the as-built WHA. This section examines these observations from thermodynamic and kinetic perspectives to provide insight into the mechanisms underlying microstructural evolution in the alloy.

The EBSD map in Fig. 6a shows a fine, equiaxed grain microstructure. The size and aspect ratio distributions in Fig. 6e, f further support this observation. Coarse and columnar grains showing an epitaxial growth along the build direction have been previously reported in LPBF of pure W. In this case, grains initially grow perpendicular to the melt pool boundary and with continued layer-wise deposition, align along the build direction, resulting in coarse and columnar microstructures [24]. However, in WHAs, the addition of Ni and Fe could lead to grain refinement of the W phase. The presence of Ni and Fe likely alters local composition and thermal gradients during solidification. This change could reduce the stability of columnar growth via constitutional supercooling and promote a columnar to equiaxed transition in the microstructure [25]. Similar refinement of W grains has been reported in the LPBF of WHAs with Ni, Fe nanoparticles, highlighting the role of alloying additions in modifying solidification pathways [26]. The observed equiaxed grain structure, with no preferential texture along all directions, may contribute to improved mechanical properties, particularly through reduced anisotropy. The Vickers hardness measurements summarized in Section 3.4 further indicate that the LPBF parameters used helped reduce anisotropy in the specimen.

The observation of Ni-Fe solute enriched regions, as presented in Fig. 8(b) could be a consequence of Ni and Fe having low solubility in W. Based on the W-Ni and W-Fe binary equilibrium phase diagrams, Ni has a maximum solubility of 0.3 at% in W, while Fe has a maximum solubility of 2.5 at% [14,15]. Thus, it is likely that Ni-Fe was rejected by the W phase under the high cooling rates of LPBF, resulting in the formation of nanoscale Ni-Fe solute enriched regions. While such nanoscale solute enriched regions have not been reported in previous studies on WHAs fabricated using conventional techniques like LPS, previous research on

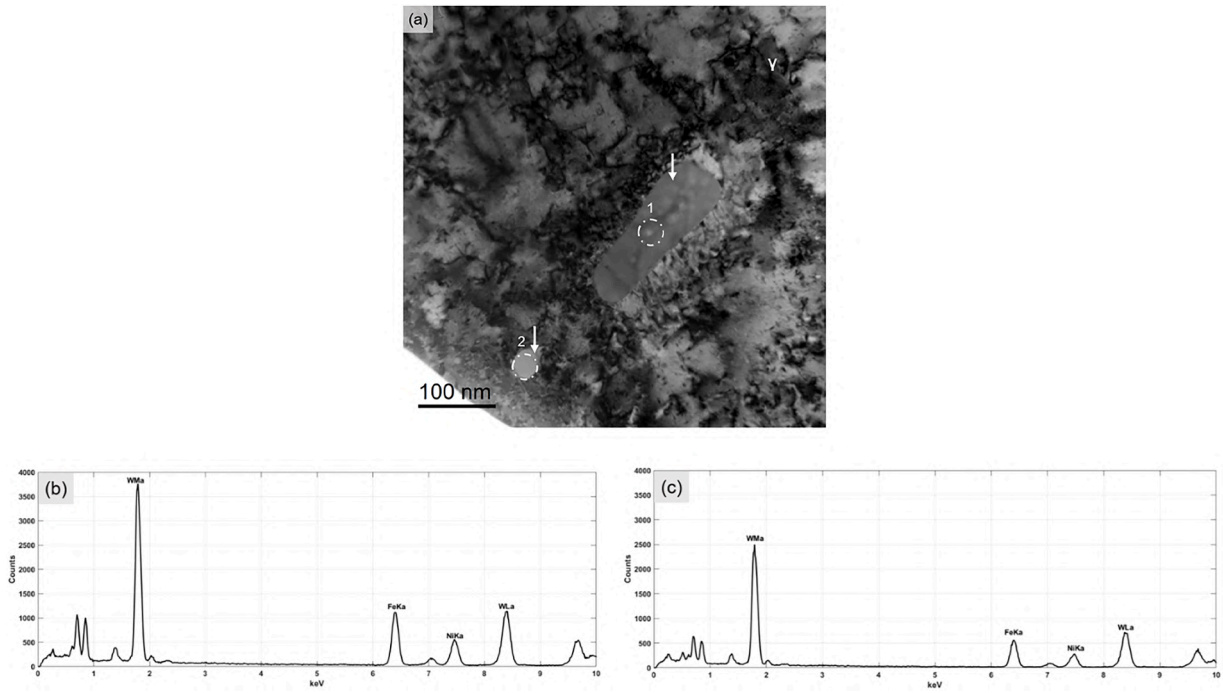


Fig. 10. (a) TEM BF image showing W rich precipitates in the γ matrix, highlighted by arrows. Dash-dot circles represent EDS spots (b) EDS spectrum from spot 1 (c) EDS spectrum from spot 2.

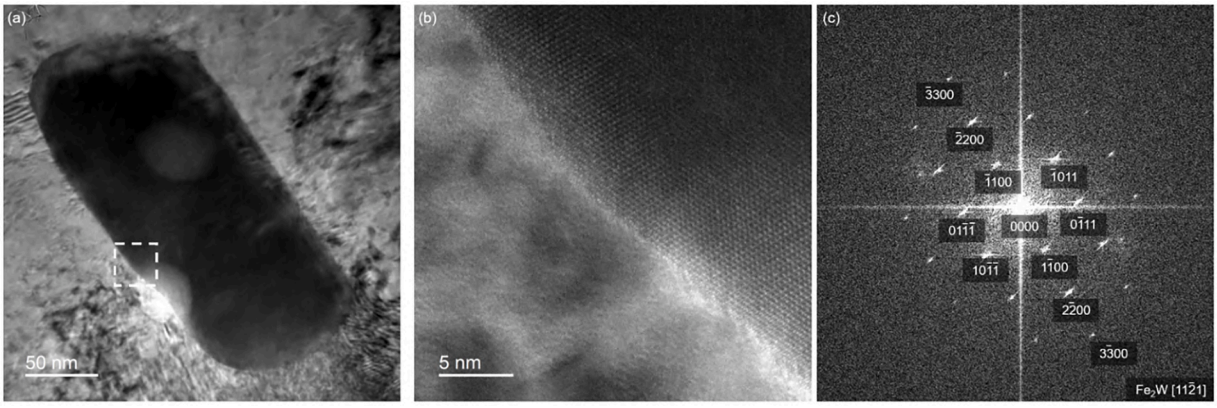


Fig. 11. (a) TEM BF image of Fe_2W precipitate (b) HRTEM image showing lattice fringes from the region highlighted by the dotted box in (a) (c) Corresponding FFT pattern.

Table 1
Summary of Vickers hardness values of 90W-7Ni-3Fe WHAs from literature.

Authors	Fabrication Method	Reported Bulk HV
Alam et al. [20]	LPS	310
Zhu et al. [21]	Vacuum sintered	226
Alam and Odette [22]	LPS	321
Mondal et al. [23]	LPS	329
	Microwave sintering	352
Wang et al. [4]	LPS	317
Present work (average of the two planes)	LPBF	358

the LPBF of an immiscible Cu-Fe-P system has shown that solute rejection due to low solubility of Fe in Cu occurs as a result of a steep decrease in temperature. It was reported that the rapid thermal quench during LPBF traps excess solute Cu inside liquid Fe-P droplets, leading to liquid phase separation with further cooling [27]. Similarly, in the present WHA system, the rejected Ni-Fe solute atoms are likely trapped in a metastable, non-equilibrium solid solution during solidification. The heating and cooling cycle from depositing subsequent layers and high-velocity Marangoni convection further promote solute atom rejection and their coalescence into fine, nanoscale solute enriched regions.

These solute enriched regions did not exhibit structural features in the SAED patterns acquired from this area, implying that the solute atoms are either incorporated into the W lattice as a substitutional solid solution or are present as BCC Ni-Fe-rich precipitation that are nearly coherent with the W lattice. Consequently, these solute enriched regions cause W lattice distortion, resulting in the formation of dislocations to accommodate the lattice strain, as observed in Fig. 8(b). Ultimately, these features could act as barriers to dislocation motion and add to WHA strength via solid solution strengthening when the material undergoes deformation.

In WHAs fabricated via PM techniques, Haag et al. previously re-

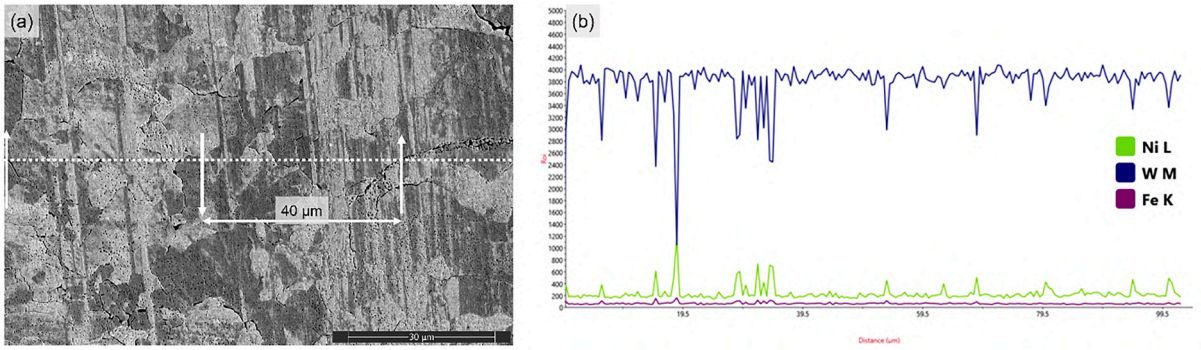


Fig. 12. (a) SEM SE image showing the EDS line scan path (indicated by the dotted line). The solid arrows indicate the LPBF hatch spacing of 40 µm to estimate the location of melt pool zones (b) Corresponding elemental EDS line scan.

ported W diffusion in the γ phase in thermo-mechanically treated LPS WHAs and further proposed that the W- γ matrix interphase boundary regions form a diffusion couple between the two phases, following the Cahn-Hilliard approach. These regions being energetically favorable were said to contribute to strengthening by increasing the energy needed for the boundary to fracture [28]. However, in LPBF WHAs, diffusion of W is less likely to occur because of the rapid solidification rate (of the order of 10^7 K/s [29]) leaving insufficient time for W atoms to diffuse into the γ matrix. Alternatively, the presence of W in the matrix could possibly be a result of the liquid γ phase encapsulating W particles during melting and solidification. Given that the melting temperature of the γ matrix is lower than that of W, it is likely that the liquid γ phase forms early during laser exposure, while W particles may remain un-melted or partially melted. The liquid γ phase could encapsulate some of these W particles and solidify together, resulting in the incorporation of W into the matrix.

Further, the presence of W in the γ matrix led to the formation of Fe_2W precipitates in the matrix, as observed in Figs. 10 and 11. Fe_2W is a known stable phase, as per both the binary W-Fe [15] and the ternary W-Ni-Fe [30] equilibrium phase diagrams, forming at temperatures of around 1060 °C in the binary system and 1020 °C in the ternary system. While LPBF is not an equilibrium process, it is possible that local equilibrium was attained during solidification, which suggests that there could be a local variation in the W:Ni:Fe composition in the specimen. These conditions could then locally promote nucleation and growth of these precipitates as Fe_2W precipitates were not observed in all γ matrix regions. The changes in the local composition and equilibrium conditions could be caused by repeated heating and solidification with the deposition of subsequent layers, leading to different amounts of W encapsulation in the liquid γ phase. Further, the high velocity and change in direction of convection caused due to high temperature gradients and laser movement, could explain the observed non-uniformity in the microstructure.

Fe_2W is a Laves phase known to be brittle, given the strong covalent nature of the Fe-W bond. Further, the Fe-W bond is intrinsically weak, which makes it susceptible to damage under stress [31]. However, when present as nano-sized precipitates in the γ matrix, the Fe_2W phase could contribute toward material strengthening. Fe_2W precipitates, about 200- 600 nm in size, were observed in Fe-W binary composite alloys fabricated using LMD and these precipitates were reported to contribute toward its high compressive yield strength [32]. Additionally, nanoscale W containing Laves phases in heat resistant steels have been reported to positively influence alloy strengthening by pinning and obstructing dislocation motion upon deformation [33,34].

Given that the formation of the Fe_2W precipitates was not intentionally targeted, but rather is a consequence of the LPBF process, the observed volume fraction of these precipitates is relatively low in the present work. The low volume fraction of these precipitates is reflected by the fact that the XRD spectrum (Fig. 3) did not show sharp Fe_2W peaks. Further, its contribution to the bulk mechanical response remains to be experimentally established. However, based on previous research highlighting the influence of Laves phases on alloy strengthening, it is likely that the fine Fe_2W nano- precipitates (100- 200 nm in size) observed in the present work could similarly impede dislocations and assist with WHA strengthening through Orowan strengthening. Fe_2W precipitates were not observed in previous studies on PM WHAs [8,28]. Their formation in AM-fabricated WHAs may therefore represent a potential microstructural advantage of AM processing. An in-depth investigation of the interactions between Fe_2W precipitates and dislocations would provide a basis for tailoring the LPBF processing conditions to promote or suppress Fe_2W formation, depending on the desired alloy performance.

Table 1 suggests that the WHA fabricated in this work shows an overall improved Vickers hardness to its conventionally fabricated counterparts. However, the measured values reflect the integrated contributions of the various microstructural features, such as the Fe_2W precipitates and solute-enriched regions, observed in the present work. It is challenging at this stage to separate the contribution of individual features based solely on these results. Therefore, HRTEM analyses and in-situ TEM mechanical testing will be required to establish a direct link between microstructure and mechanical response.

Thus, the overall influence of the observed microstructural features on the mechanical behavior of AM WHAs is yet to be validated. Additionally, the influence of different LPBF scan strategies on the microstructure and performance remains unanswered. A bidirectional scanning strategy with a misorientation of 67° between consecutive layers is the most widely used scan strategy across various LPBF studies to mitigate defects and residual stresses. However, using alternative scan strategies such as a parallel (interlayer misorientation of 0°) scan strategy or bidirectional scanning with an interlayer misorientation of 90°, could be beneficial to test the ability of AM parameters to fine tune the microstructure of WHAs. These open questions will be addressed in future work.

5. Conclusion

This study presented a multiscale characterization of a 90W-7Ni-3Fe WHA fabricated using LPBF with the overarching goal of understanding the link between the processing- microstructure- performance of these alloys. The non-equilibrium, rapid solidification microstructure was characterized at the micro and nanoscales using SEM and TEM and the following characteristics were observed:

i. A two-phase microstructure was observed with W embedded in a Ni-Fe γ phase matrix, separated into two distinct regions – a homogenous region with completely melted W and the other with un-melted W particles. W dendrites were primarily found to be present in regions with un-melted W particles, while submicron

scale γ precipitates were observed in W grains. These observations suggest non- uniform, location dependent laser melting.

ii. Clear melt pool boundaries were not visible, and their absence was attributed to complete melting and homogenous solidification, and the alloy not showing elemental segregation because of high W content.

iii. The absence of a preferential texture in the specimen, along with the measured Vickers hardness values on different specimen planes, suggest that the specimen shows reduced anisotropy.

iv. A fine, equiaxed grain structure was seen, as opposed to the coarse, columnar grain structure reported in LPBF of pure W. The columnar to equiaxed transition could be promoted by the addition of Ni and Fe to W.

v. Processing defects such as pores were reported at the SEM scale and TEM analysis revealed that γ precipitates could be favorable sites for porosity. These pores could be sites prone to failure during deformation.

vi. A high dislocation density was observed in EBSD misorientation and TEM analysis, suggesting that the WHA experiences thermal stresses during rapid solidification. Further, nanosized Ni-Fe solute enriched regions were observed in W grains especially where the dislocation density was high. It is hypothesized that these solute enriched regions could lead to solid solution or solute cluster strengthening of the WHA.

vii. W was found to be incorporated in the γ matrix, resulting in γ lattice expansion. Further, nanoscale Fe_2W precipitates were found in some γ regions. The observation of W in γ and the Fe_2W precipitates could be indicators of variations in local composition and solidification kinetics during LPBF. Further, these nanosized Fe_2W precipitates could contribute to WHA strengthening by pinning and/or hindering dislocations.

The observed nanoscale microstructural features, including solute enrichment and intermetallic phase formation within grains, were absent in both our prior LPS experiments and previous laser-based sintering studies. This demonstrates that LPBF produces fundamentally distinct microstructural evolution, characterized by previously unreported nanoscale heterogeneities arising from strongly non-equilibrium processing conditions. The insight presented in this work will be utilized to understand the influence of microstructure on the mechanical behavior of AM WHAs, which will subsequently help guide microstructure design of these alloys.

CRediT authorship contribution statement

Anugrahaprada Mukundan: Writing – original draft, Investigation, Formal analysis, Data curation. **Ryosuke Ozasa:** Writing – review & editing, Resources, Methodology, Data curation. **Takayoshi Nakano:** Supervision, Methodology, Funding acquisition. **Mitsuhiro Murayama:** Writing – review & editing, Supervision, Resources, Methodology, Funding acquisition, Conceptualization.

Declaration of Competing Interest

The authors declare that they have no known competing financial interests or personal relationships that could have appeared to influence the work reported in this paper.

Acknowledgments

This work used shared facilities at the Nanoscale Characterization and Fabrication Laboratory, which is funded and managed by Virginia Tech's Institute for Critical Technology and Applied Science. Additional support is provided by JSPS KAKENHI (Grant Numbers: 23H00238, 23H00235 and 25K00051), CREST-Nanomechanics: Elucidation of macroscale mechanical properties based on understanding the nanoscale dynamics of innovative mechanical materials (Grant Number: JPMJCR2194), and the Virginia Tech National Center for Earth and Environmental Nanotechnology Infrastructure (NanoEarth), a member of the National Nanotechnology Coordinated Infrastructure (NNCI), supported by NSF (ECCS 2025151).

Supplementary materials

Supplementary material associated with this article can be found, in the online version, at doi:10.1016/j.mtla.2026.102940.

References

[1] N. Senthilnathan, A. Raja Annamalai, G. Venkatachalam, Sintering of tungsten and tungsten heavy alloys of W–Ni–Fe and W–Ni–Cu: a review, Trans. Indian Inst. Met. 70 (2017) 1161–1176, https://doi.org/10.1007/s12666-016-0936-2.

[2] M.C. Brennan, J.S. Keist, T.A. Palmer, Defects in metal additive manufacturing processes, J. Mater. Eng. Perform. 30 (2021) 4808–4818, https://doi.org/10.1007/s11665-021-05919-6.

[3] A. Iveković, M.L. Montero-Sistiaga, K. Vanmeensel, J.-P. Kruth, J. Vleugels, Effect of processing parameters on microstructure and properties of tungsten heavy alloys fabricated by SLM, Int. J. Refract. Met. Hard Mater. 82 (2019) 23–30, https://doi.org/10.1016/j.ijrmhm.2019.03.020.

[4] Y.P. Wang, S.Y. Ma, X.S. Yang, Y.Z. Zhou, X. Liu, J.F. Li, J.J. Zhang, C. Li, X. Y. Wang, G.M. Le, Y. Zhang, Microstructure and strengthening mechanisms of 90W–7Ni–3Fe alloys prepared using laser melting deposition, J. Alloys Compd. 838 (2020) 155545, https://doi.org/10.1016/j.jallcom.2020.155545.

[5] T. Schwanekamp, A. Müller, M. Reuber, H. Gobran, N. Gdoura, S. von Cetto, Investigations on laser powder bed fusion of tungsten heavy alloys, Int. J. Refract. Met. Hard Mater. 109 (2022) 105959, https://doi.org/10.1016/j.ijrmhm.2022.105959.

[6] T.W. Verdonik, M. Pires, T.-S. Guo, N. Rockwell, W.Z. Misiolek, Investigation of powder bed laser fusion additive manufacturing of 93W, 5.6Ni, 1.4Fe tungsten heavy alloys, Int. J. Refract. Met. Hard Mater. 111 (2023) 106055, https://doi.org/10.1016/j.ijrmhm.2022.106055.

[7] D. Dai, L. Wang, T. Chen, K. Shi, H. Zhang, Dual-laser powder bed fusion of difficult-to-process tungsten heavy-alloy: inhibition of inferior defects and integrated fabrication of thin-walled overhanging structures, Thin-Walled Struct. 208 (2025) 112827, https://doi.org/10.1016/j.tws.2024.112827.

[8] J.V. Haag, D.J. Edwards, C.H. Henager, W. Setyawan, J. Wang, M. Murayama, Characterization of ductile phase toughening mechanisms in a hot-rolled tungsten heavy alloy, Acta Mater. 204 (2021) 116523, https://doi.org/10.1016/j.actamat.2020.116523.

[9] R.D. Li, J.H. Liu, Y.S. Shi, L. Zhang, M.Z. Du, Effects of processing parameters on rapid manufacturing 90W–7Ni–3Fe parts via selective laser melting, Powder Met. 53 (2010) 310–317, https://doi.org/10.1179/174329009X442726.

[10] S. Omole, A. Lunt, S. Kirk, A. Shokrani, Advanced processing and machining of tungsten and its alloys, J. Manuf. Mater. Process. 6 (2022) 15, https://doi.org/10.3390/jmmp6010015.

[11] B. Chen, Y. Guo, S. Li, G. Liu, Experimental study on laser ablation texture-assisted grinding of tungsten alloy, Mater 15 (2022) 7028, https://doi.org/10.3390/ma15197028. . (Basel).

[12] C. Wei, H. Ye, Z. Zhao, J. Tang, X. Shen, G. Le, K. Ye, F. Le, Microstructure and fracture behavior of 90W-7Ni-3Fe alloy fabricated by laser directed energy deposition, J. Alloys Compd. 865 (2021) 158975, https://doi.org/10.1016/j.jallcom.2021.158975.

[13] E. Fortuna, W. Zielinski, K. Sikorski, K.J. Kurzydlowski, TEM characterization of the microstructure of a tungsten heavy alloy, Mater. Chem. Phys. 81 (2003) 469–471, https://doi.org/10.1016/S0254-0584(03)00055-5.

[14] H. Okamoto, Ni-W (Nickel-Tungsten), J. Ph. Equilibria 12 (6) (1991) 706, https://doi.org/10.1007/BF02645185.

[15] O.K. von Goldbeck, Fe-W iron-tungsten. IRON - Bin. Phase Diagrams, Springer, Verlag Berlin Heidelberg, 1982, pp. 164–167, https://doi.org/10.1007/978-3-662-08024-5_76.

[16] J. Li, Z. Wei, B. Zhou, Y. Wu, S. Chen, Z. Sun, Densification, microstructure and properties of 90W-7Ni-3Fe fabricated by selective laser melting, Metals 9 (2019) 884, https://doi.org/10.3390/met9080884 (Basel).

[17] M. Ameri, D. Rached, M. Rabah, R. Khenata, N. Benkhettou, B. Bouhafs, M. Maachou, Structural and electronic properties calculations of BexZn1−xSe alloy, Mater. Sci. Semicond. Process. 10 (2007) 6–13, https://doi.org/10.1016/j.mssp.2007.01.003.

[18] G. Cacciamani, J. De Keyzer, R. Ferro, U.E. Klotz, J. Lacaze, P. Wollants, Critical evaluation of the Fe–Ni, Fe–Ti and Fe–Ni–Ti alloy systems, Intermetallics 14 (2006) 1312–1325, https://doi.org/10.1016/j.intermet.2005.11.028.

[19] N. Asrar, L.L. Meshkov, E.M. Sokolovskaya, Phase equilibria in ternary alloys metals and containing refractory metals (Mo, W, Nb, Ta), J. Less-Common Met. 144 (1988) 41–52.

[20] M.E. Alam, J. Wang, C.H. Henager, W. Setyawan, G.R. Odette, The effect of hot rolling on the strength and fracture toughness of 90W–7Ni3Fe tungsten heavy metal alloys, Mater. Sci. Eng. A. 824 (2021) 141738, https://doi.org/10.1016/j.msea.2021.141738.

[21] W. Zhu, Y. Ma, W. Liu, Q. Cai, Y. Huang, Z. Wen, Study on low-temperature sintering behavior of 90W-7Ni-3Fe alloys: the influence of Sn addition, J. Mater. Eng. Perform. 29 (2020) 5894–5901, https://doi.org/10.1007/s11665-020-05055-7.
[22] M.E. Alam, G. Odette, On the remarkable fracture toughness of 90 to 97W-NiFe alloys revealing powerful new ductile phase toughening mechanisms, Acta Mater. 186 (2020) 324–340, https://doi.org/10.1016/j.actamat.2020.01.012.
[23] A. Mondal, A. Upadhyaya, D. Agrawal, Effect of heating mode and sintering temperature on the consolidation of 90W-7Ni-3Fe alloys, J. Alloys Compd. 509 (2011) 301–310, https://doi.org/10.1016/j.jallcom.2010.09.008.
[24] D. Gu, M. Guo, H. Zhang, Y. Sun, R. Wang, L. Zhang, Effects of laser scanning strategies on selective laser melting of pure tungsten, Int. J. Extrem. Manuf. 2 (2020) 025001, https://doi.org/10.1088/2631-7990/ab7b00.
[25] D.A. Porter, K.E. Easterling, Phase Transformations in Metals and Alloys, 2nd ed., 1992.
[26] M. Guo, K. Liu, J. Sun, D. Gu, Laser powder bed fusion of a novel nano-modified tungsten alloy with refined microstructure and enhanced strength, Mater. Sci. Eng. A. 843 (2022) 143096, https://doi.org/10.1016/j.msea.2022.143096.
[27] C. Wen, Y. Qiu, Z. Zhang, K. Li, C. Deng, L. Hu, Deformation behavior of heterogeneous lamellar Cu-Fe-P immiscible alloys with enhanced strength and ductility produced by laser powder bed fusion, 971 (2024) 172675. 10.1016/j.jallcom.2023.172675.
[28] J.V Haag, J. Wang, K. Kruska, M.J. Olszta, C.H. Henager, D.J. Edwards, W. Setyawan, M. Murayama, Investigation of interfacial strength in nacre-mimicking tungsten heavy alloys for nuclear fusion applications, Sci. Rep. 13 (2023) 575, https://doi.org/10.1038/s41598-022-26574-4.
[29] T. Todo, T. Ishimoto, O. Gokcekaya, J. Oh, T. Nakano, Single crystalline-like crystallographic texture formation of pure tungsten through laser powder bed fusion, Scr. Mater. 206 (2022) 114252, https://doi.org/10.1016/j.scriptamat.2021.114252.
[30] F.R. Winslow, The Iron-Nickel-Tungsten Phase Diagram, U.S. Atomic Energy Commission, 1971, https://doi.org/10.2172/4014855.
[31] C. Lu, Y. Wang, X. Lei, J. Yang, J. Huang, S. Chen, Y. Zhao, Influence of Fe-W intermetallic compound on fracture behavior of steel/tungsten hip diffusion bonding joint: experimental investigation and first-principles calculation, J. Manuf. Process. 55 (2020) 131–142, https://doi.org/10.1016/j.jmapro.2020.03.054.
[32] H. Chen, L. Ye, Y. Han, C. Chen, J. Fan, Additive manufacturing of W–Fe composites using laser metal deposition: microstructure, phase transformation, and mechanical properties, Mater. Sci. Eng. A. 811 (2021) 141036, https://doi.org/10.1016/j.msea.2021.141036.
[33] J.P. Sanhueza, D. Rojas, O. Prat, J. Garcia, M.F. Melendrez, S. Suarez, Investigation of Ta-MX /Z-phase and laves phase as precipitation hardening particles in a 12 pct Cr heat-resistant steel, Met. Mater. Trans. A-PHYS. Met. Mater. Sci. 49 (2018) 2951–2962, https://doi.org/10.1007/s11661-018-4654-8.
[34] O. Prat, J. Garcia, D. Rojas, G. Sauthoff, G. Inden, The role of laves phase on microstructure evolution and creep strength of novel 9 % Cr heat resistant steels, Intermetallics 32 (2013) 362–372, https://doi.org/10.1016/j.intermet.2012.08.016.